Precipitation Evolution and Modeling of Growth Kinetics of L1$_2$-structured Al$_3$Zr Particles in Al-0.22Zr and Al-0.32Zr (wt.%) Alloys Isothermally Aged

Pedro Henrique Lamarão Souza[a]*, José Maria do Vale Quaresma[b], Carlos Augusto Silva de Oliveira[a]

[a]Universidade Federal de Santa Catarina - UFSC, Campus Universitário João David Ferreira Lima, Rua Delfino Conti, Trindade, CEP: 88040-900, Florianópolis, SC, Brasil.
[b]Universidade Federal do Pará - UFPA, Campus Guamá, Rua Augusto Corrêa, nº 01, Guamá, CP 479, CEP: 66075-110, Belém, PA, Brasil.

The microstructure and microhardness of isothermally aged Al-0.22Zr and Al-0.32Zr alloys were investigated. Peak microhardness occurred after aging at 650K for 100 h for both alloys and decreased slightly after aging at 400 h. Nanometer-scale spherical L1$_2$-structured Al$_3$Zr precipitates were observed using Transmission Electron Microscopy, these presented r < 7 nm at the center of dendrite branches. In the Al-0.32Zr alloy, particles increased in radius after aging at 650 K from 100 to 400 h while in the Al-0.22Zr alloy, precipitate radii remained constant in the same range. This is possibly due to solute migration to the periphery of dendritic branches, where larger particles nucleated. After aging at 700 K for 100h, there are growth instabilities at the interface of the particles. A theoretical model, used to predict particle growth by diffusion, presented good agreement with the experimental findings.

Keywords: *Microstructure, Al-Zr alloys, L1$_2$-structured Al$_3$Zr precipitates, particle growth, microhardness.*

1. Introduction

Studies about cast and aged Al-Zr alloys aim applications at elevated temperatures, in the production of automotive and aeronautical components[1]. In the former, cast Al alloys are employed in pistons, cranckshafts, air-cooled cylinder heads and gear housings. In the latter as pylons and missile tail cones[2].

Al-Zr alloys are precipitation hardening and present elevated thermal stability due to the precipitation of nanometer-scale metastable Al$_3$Zr L1$_2$ precipitates[1,3,4]. These particles are coherent, thermodynamically stable[5] and provide hardening even after long times of heat-treatment (400 h) at temperatures of 698 K[6] and nucleate homogeneously in a high number density at the center of the dendrites, where supersaturation is greater[4,6]. Al$_3$Zr precipitates present a series of different morphologies, depending on processing conditions these may be spheroidal[6-8], rod-like[6,8], petal-like[6,9,10], cauliflower[6], cellular[11,12] and disk-like[13,14].

In Al-Zr alloys of hypoperitectic compositions (wt.% Zr < 0.28)[15], Ness[8] showed that after aging at 733 K, an Al-0.18wt.%Zr alloy presented L1$_2$-structured Al$_3$Zr particles, that increased in size from ~20 to 70 nm in the range of 24 - 700 h of aging time. The authors observed spherical particles mainly, although some rod-like particles are present in ⟨100⟩ matrix directions.

Some authors[6,9-12,14] had performed microstructural characterization in hyperperitectic Al-Zr alloys and observed that the main particles responsible for hardening are the spherical Al$_3$Zr, nucleated at the center of dendrite branches, while the rod-like and cauliflower morphologies occur at solute depleted regions[6]. The petal-like morphology is characteristic of coarse particles that nucleate during solidification in slowly cooled Al-Zr alloys. They nucleate at high temperatures, and its presence is undesirable for mechanical properties, once they deplete the matrix with Zr[4]. The cellular morphology is associated with the discontinuous precipitation of Al$_3$Zr along a moving grain boundary[12,14]. It was observed after aging at 773 K for 120 h in an Al-0.5wt.%Zr alloy[11] and after aging at the same temperature for 3 h in an Al-9.4wt.%Zr alloy[12]. The disk-like morphology is the equilibrium tetragonal D0$_{23}$ structure, which nucleates after aging at temperatures above 773 K[13,14,16].

The precipitation of L1$_2$-structured Al$_3$Zr particles is modified by the presence of ternary additions. Yb additions promote a two-peak hardening during isochronal aging, by the precipitation of L1$_2$-structured Al$_3$(Zr,Yb) precipitates, that are more coarsening-resistant than Al$_3$Zr or Al$_3$Yb particles[17]. Y additions accelerate the precipitation kinetics of Al$_3$Zr particles and retard coarsening[18].

In quaternary alloys, the combined effect of Zr, Sc and Er in Al alloys precipitate the L1$_2$-structured Al$_3$(Zr,Sc,Er) precipitate, which present a core-shell structure and provide hardening for periods as 64 days of aging at 673 K[1]. Booth-morrison et al.[19] studied the effects of Er additions in the quaternary Al-Zr-Sc-Si alloy. It was observed that coarsening and creep resistance at 673 K increased with the presence of Er intermetallics.[20] studied an Al-Mn-Sc-Zr aged at 573 K. Although appreciable hardening was observed by the presence

*e-mail: pedro.lamarao@posgrad.ufsc.br.

of L1$_2$-structured Al$_3$(Sc,Zr) particles, Mn solutes were not observed in the precipitation process.

Lefebvre et al.[21] studied Al$_3$Zr precipitation in an Al-0.34Zr alloy with the presence of Fe and Si from a 1050 Al alloy. No discussions of the influence of Fe and Si over the precipitation of the L1$_2$-structured Al$_3$Zr particles were performed, although the authors were the first to study the shearing to bypassing transition of the particles by dislocations.

There is little information quantifying the microstructural evolution at the center and periphery of dendrite branches during isothermal aging. As already explained by Knipling et al[6], Al-Zr alloys present strong solute segregation along dendrites. This gives rise to a range of particle size distributions at distinct regions during aging. Also, there is little information about the mechanical properties of hypoperitectic Al-Zr alloys and few papers had proposed modeling for the prediction of the growth kinetics of L1$_2$-structured Al$_3$Zr particles during aging. Therefore, this study investigates the microstructures of dilute Al-0.22wt.%Zr and Al-0.32wt.%Zr alloys after isothermal aging and correlate this information with its Vickers microhardness and with a theoretical model consisting of equations from solidification, nucleation and diffusional growth that simulate the evolution of precipitate radii with time.

2. Experimental

The alloys were conventionally cast, using high purity Al (99.8 %) and an Al-10Zr master alloy (all compositions in wt.%). Conventional casting occurred inserting the metals in a kaolin coated SiC crucible and casting in a resistively heated furnace at 1120 K. Subsequently the melt was stirred, degassed with inert gas (Ar) and poured in a water-cooled Cu mold, producing an ingot weighting ~ 600 g.

Table 1 presents the chemical composition of the alloys. The Al-0.22Zr alloy was analyzed in a Bruker Q4 Tasman Optical Mass Spectrometer and the Al-0.32Zr alloy in a Perkin Elmer Optima 8300 Inductively Coupled Plasma Optical Emission Spectrometer.

The samples were isothermally aged using a resistively heated furnace. The temperatures employed were 650 and 700 K, ±1K at the times of 4, 12, 24, 100 and 400 h. The aging temperatures and times were adopted because a study in the literature demonstrated that these parameters promote precipitation hardening in hiperperitectic Al-Zr alloys[4]. After the treatments, samples were water-quenched to room temperature.

Vickers microhardness tests were performed in accordance with the ASTM E384[22] standard; using a load of 1.96 N

(200 gf) and a dwelling time of 5 s. 20 microhardness tests were performed at each sample.

The as-cast microstructure of the alloys was investigated using Scanning Electron Microscopy - SEM using Backscattered Electrons - BSE for imaging and Energy Dispersive X-ray Spectroscopy - EDS for analysis of dispersoids and chemical composition in the matrix.

The microstructures of the specimens were analyzed by Transmission Electron Microscopy - TEM, using a JEOL JEM 1011 microscope, with an accelerating voltage of 100kV, employing bright-field, dark-field and Selected Area Diffraction - SADP techniques.

The samples for TEM analysis were grinded to 100 μm thickness discs and thinned to perforation in a Struers Tenupol 5 electropolishing unit, using an electrolyte of 2/3 methyl alcohol and 1/3 nitric acid at the temperature of 276 K ±3 K. After electropolishing, cleaning of the samples occurred by rinsing it three times into methanol and in methyl alcohol, a procedure similar to the one used by Ünlü[23].

In the TEM, precipitate radii were measured at the center and periphery of dendrite branches. The former being regions with an apparent higher number density of smaller particles and the latter with an apparent lower number density of bigger particles and also with the presence of rod-like precipitates. Several independent micrographs were recorded to obtain reliable results. Precipitate radii were measured using software ImageJ, the results were exported to the software R statistical to remove outliers and to calculate descriptive statistics as precipitate mean radii - ⟨r⟩. The indexing of the SADPs was realized using the software Web E-MAPS, which simulated the diffraction conditions used in the present study.

3. Modelling Precipitation Kinetics

In the present study, the experimental results of ⟨r⟩ at the center of dendrite branches were compared with theoretical calculations. The model considers distinct aspects from solidification, nucleation and diffusional growth.

The first calculated parameter is the solute content at the center of dendrite branches, which is obtained from the Scheil equation for solute distribution during solidification - C_e (Eq.1), considering total mixing in the liquid and no diffusion in the solid[24], where k_0 is the solid/liquid partition coefficient (Eq.2)[24], C_0 the nominal solute concentrations of the studied alloys, f_s the solidified fraction, $C_s = 0.28$wt.%Zr the equilibrium solid solubility and $C_L = 0.11$wt.%Zr[15] the equilibrium liquid solubility.

$$C_e = k_0 C_0 \left(1 - f_s\right)^{k_0 - 1} \tag{1}$$

$$k_0 = C_S / C_L \tag{2}$$

As the solidification conditions are distinct from equilibrium, and the local Zr concentration in the ingot at

Table 1. Chemical compositions of the studied alloys.

Alloy	Zr	Fe	Si	Al
Al-0.22Zr	0.23	0.10	0.05	Balance
Al-0.32Zr	0.32	0.10	0.03	Balance

the metal/mold interface may differ from the innermost regions, both C_0 and k_0 were fitted simulating values from 0.1 to 0.8 wt.%Zr for C_0 and from 1.00 to 2.54 for k_0. The values that obtained the minimum Residual Sum of Squares - RSS (Eq.3)[25] were selected for the next calculation steps. In Eq.3, C_{exp} is the Zr concentration measured along the sample and the i superscripts indicate the number of data points.

$$RSS = \sum_{i=1}^{n}(C_{exp}^{i} - C_{e}^{i})^{2} \qquad (3)$$

As f_s varies from 0 to 1, where the former value is the center of dendrite branch and the latter the periphery of dendrite branches. It is considered, for modeling purposes, that the Zr concentration at the center of dendrite branches - C_m is equal to C_e for $f_s = 0.01$.

The next calculation step was the determination of the critical radius for nucleation - r^*, assuming that homogeneous nucleation occurs at the center of dendrite branches. The values for r^* are calculated in Eq. (4)[26], where $\gamma = 0.1033$ J/m^2 [27] is the interfacial energy of the Al$_3$Zr L1$_2$ precipitate with the Al matrix at 650 K, V_a is the atomic volume, $k = 1.381E-23$ J/K is the Boltzman constant[28], $R = 8,314$ kJ/mol the universal gas constant[28], T the absolute temperature and $C_\alpha^{L1_2}$ (Eq.5)[4] is the Zr concentration in the matrix in equilibrium with the Al$_3$Zr particle and is calculated from the *solvus* line of the metastable Al$_3$Zr L1$_2$, where $C_\alpha^{D0_{23}}$ is the equilibrium *solvus* (Eq.6)[29].

$$r^* = 2\gamma V_a / kT \ln(C_m / C_\alpha^{L1_2}) \qquad (4)$$

$$C_\alpha^{L1_2} = C_\alpha^{D0_{23}} \cdot 0.710 \cdot exp(1300/T) \qquad (5)$$

$$C_\alpha^{D0_{23}} = 1180 \cdot exp(-64.96 \cdot 10^3 / RT) \qquad (6)$$

This calculation step considers that the metastable L1$_2$-structured Al$_3$Zr particle has its stoichiometric composition and no other intermetallic compounds consume Zr from the matrix. Also, during nucleation, the Zr concentration at the precipitate/matrix interface is equal to the solute concentration in the matrix at the center of dendrite branches[26].

The variation of particle radius considering diffusion control - r_d is expressed in Eq. (7)[30], C_β is the Zr content in the particle, Ω is the dimensionless supersaturation (Eq. 8), D is the diffusion coefficient (Eq. (9))[31], where $D_0 = 7.28 \times 10E-02$ m^2/s and $Q = 241.8$ kJ/mol are the pre-exponential factor and the activation enthalpy for diffusion, respectively[32] and t is the time.

$$r_d = (2\Omega D t)^{1/2} \qquad (7)$$

$$\Omega = (C_m - C_\alpha^{GT}) / (C_\beta - C_\alpha^{GT}) \qquad (8)$$

$$D = D_0 \, exp(-Q/RT) \qquad (9)$$

In Eq. 8, C_m varies with time due to precipitation, because the particles drain solute from the matrix as they grow - C_m (t) (Eq.10)[33,34], where τ is a temperature-dependent factor (Eq. 11[33]) and λ the experimental interparticle spacing. The variable C_α^{GT} (Eq. 12)[35] is the metastable solubility corrected for capillarity effects, where V_m is the molar volume.

$$C_m(t) = C_\alpha^{GT} + (C_m - C_\alpha^{GT}) exp(-t/\tau) \qquad (10)$$

$$\tau = ((\lambda/2)^2 / 2D)(C_\beta / C_m)^{1/3} \qquad (11)$$

$$C_\alpha^{GT} = C_\alpha^{L1_2} exp(2\gamma V_m / rRT) \qquad (12)$$

When $r^* \to 0$, the variation of r with time can be expressed using Eq.7[30] otherwise it is computed considering the sum of r^* (Eq.4) and r_d (Eq.7), in Eq.13[34,36], where r_m is the particle radius of the model.

$$r_m = r^* + r_d \qquad (13)$$

The main limitations of the model are that: (i) solute gradients along the dendrite branches are not considered; (ii) competitive growth, which might appear after soft impingement of the diffusion fields, is not being modeled.

4 Results and Discussion

4.1 As-cast condition

Samples were studied in the as-cast condition to assess the presence - or not of primary Al$_3$Zr particles formed during solidification. Figure 1a is a TEM micrograph of the Al-0.22Zr alloy. It is possible to observe the contrast due to dislocations in the matrix only. Figure 1b is a bright field micrograph of the Al-0.32Zr alloy. Again the micrograph exhibits the presence of dislocations only.

Although TEM images of the as-cast samples did not revealed the presence of dispersoids, SEM results (Figure 2) show the presence of both primary eutectic and peritectic phases. In Figure 2a, it is possible to observe globular Al-Fe phases (arrows 1 and 2) and a Al-Fe-Si lamelar phase (arrow 3), as assessed by EDS analysis. These particles are commonly nucleated during solidification of Al alloys[37].

Figure 2b is a micrograph of the Al-0.32Zr alloy. It is also possible to observe the presence of dispersoids, in this case, possibly primary Al$_3$Zr (arrow 4), due to the presence of Al and Zr only, as indicated by its EDS spectrum in Figure 3a. Arrows 5 and 6 indicate the presence of Al, Zr and Fe (Figure 3b).

It is possible that primary Al$_3$Zr parricles are nucleating heterogeneously over Al-Fe dispersoids during solidification, because there are no equilibrium Al-Zr-Fe phases predicted by the Al rich corner of its ternary diagram. There is a study
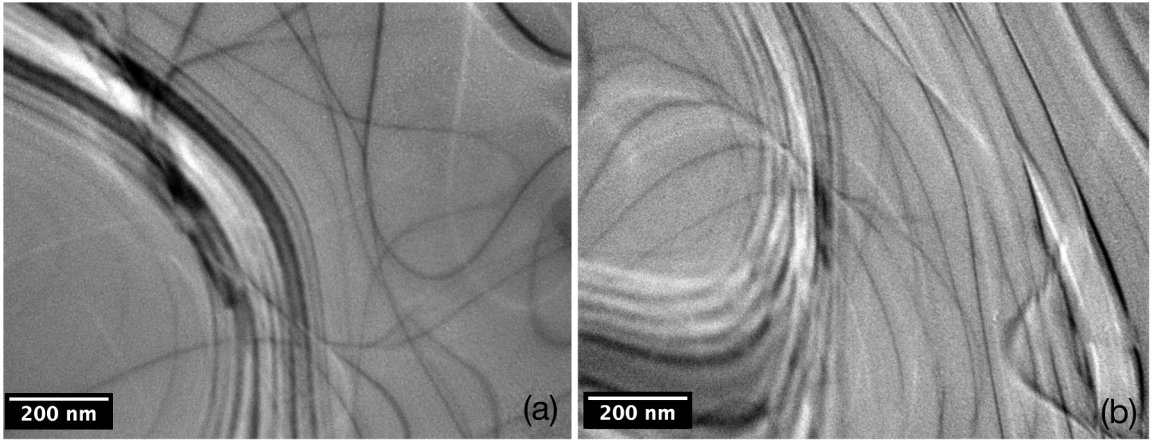
Figure 1. Bright-field TEM micrographs of as-cast samples of (a) Al-0.22Zr and (b) Al-0.32Zr alloys.
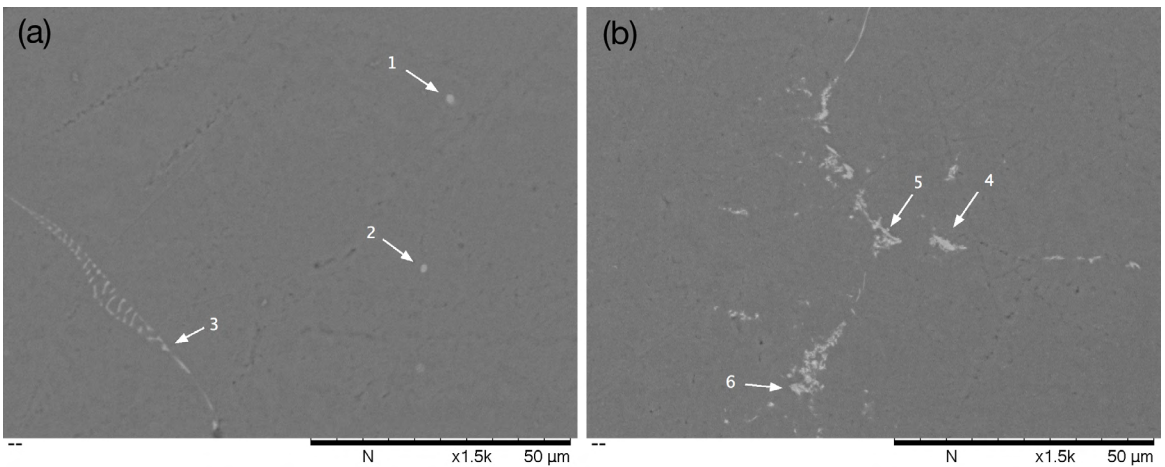
Figure 2. SEM micrographs of the as-cast alloys (a) Al-0.20Zr and (b) Al-0.32Zr.
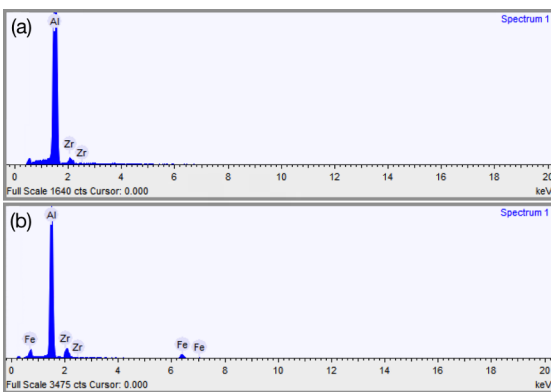
Figure 3. EDS spectrum of arrows 4 (a) and 5 (b) in Fig.2b, with the elements Al, Fe and Zr.

in the literature in an Al-25Zr-12.5Fe alloy obtained with powder metallurgy in which an Al$_{11}$Fe$_8$Zr$_6$ intermetallic was found[38].

The nucleation of primary Al$_3$Zr particles occurs in Al-Zr alloys when the solidification cooling rate is bellow

a critical value. If the cooling rate is high enough, there is peritectic suppression, which culminates with the formation of a metastable supersaturated solid solution[39]. Once the critical cooling rate for peritectic suppression reduces with lower solute content[10], this is possibly the reason why no Zr rich particles were observed in the Al-0.22Zr alloy.

The Zr content also influences in the modification of the average grain size of the alloys. In the Al-0.22Zr and Al-0.32Zr alloys, the average grain sizes are 127 and 79 μm, respectively, indicating a ~60% decrease in the average grain size due to the presence of Zr.

Inside the grains, EDS measurements were performed in order to observe the Zr segregation throughout the microstructure and use the measurements as a part of the input of the modeling process. Figure 4 exhibits results for the studied alloys. It is possible to observe that the Zr concentration present peaks, which indicates the center of dendrite branches, while the solute depleted areas are possibly the periphery of dendrite branches. Figure 4a presents lower solute concentration than Figure 4b, due to the presence of a higher Zr concentration in the Al-0.32Zr alloy. The average
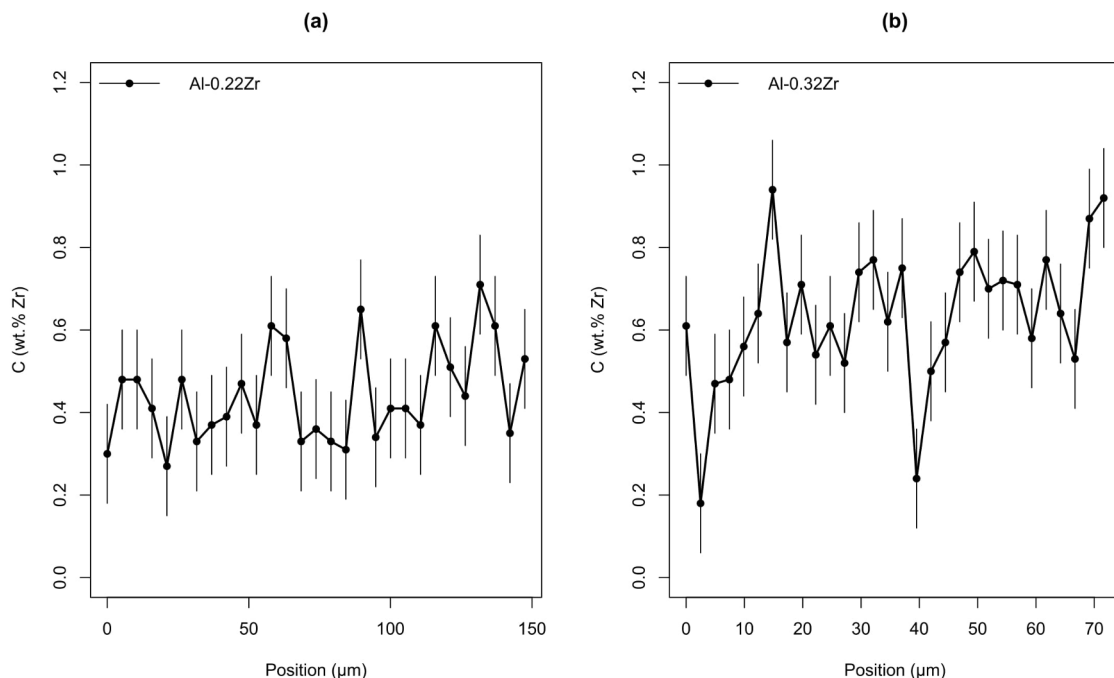
Figure 4. Zr composition along a grain in the (a) Al-0.22Zr and (b) Al-0.32Zr alloys.

Zr concentration is above the nominal solute content of the alloy, although Zr peaks are expected by the Scheil model other studies in the literature found similar results[26,40].

4.2 Age hardening

Figure 5 presents the variation of microhardness as a function of aging temperature and time. Considering the effect of temperature, in the results of the Al-0.22Zr alloy (Figure 5a), at 650 K, hardening was greater than at 700 K, regardless of the aging time. This happens because the driving force for precipitation is greater at the lower temperature[6], causing the precipitation of particles with smaller radius during aging at 650 K (section 4.3). The same behavior occurs in the Al-0.32Zr alloy (Figure 5b).

Considering the effect of aging time, in the heat-treatment of the Al-0.22Zr alloy (Figure 5a), the increase in hardness started in 12 h at 650 K, achieving peak strength in 100 h. In 400 h, there is a slight decrease in microhardness. At 700 K, samples started to harden in 24 h, reaching peak-strength in 100 h and maintaining it in 400 h. In the Al-0.32Zr alloy (Figure 5b), microhardness values started to increase at 4 h of aging at 650 K. A steep increase in hardness occurs until 24 h, after which the increment in strength slowed and the alloy achieved peak hardness at 100 h. At 400 h, there is a slight decrease in hardness. At 700 K, similar behavior happens until 24 h, although the microhardness values are lower. The increase in strength was negligible from 24 to 100 h and the decrease in microhardness was greater at 400 h.

In both studied alloys, hardening occurred in shorter times during aging at 650 K. Although diffusion increases with temperature, hence accelerating precipitation kinetics[30,35] it is possible that the number density of precipitates in the earlier times of aging at 700 K is low, provided that no increase in hardness can be observed.

Considering the effect of solute content in Figure 5, for a given aging temperature or time, microhardness values are greater in Figure 5b (Al-0.32Zr) than in Figure 5a (Al-0.22Zr). The higher solute content in the former alloy led to the formation of precipitates with lower radii than in the latter during aging (section 4.3).

The precipitation kinetics in Figure 5b is similar to the results obtained by Knipling et al.[6], which studied an alloy produced by arc-melting, with similar composition (Al-0.34Zr) and aging temperatures (648 and 698 K), although microhardness values in the present work are ~10 HV 0.2 higher. Ryum[11] studied a chill cast Al-0.5Zr alloy aged at 773 K. The alloy presented an increase in hardness of ~ 2 HV 0.3 after aging for 20 - 120 h.

4.3 Microstructural characterization of the aged alloys

Table 2 presents measurement results of the particles found in the micrographs. Several independent measurements were realized to obtain particle mean values. Figure 6 present results of measurements of sample aged at 650 K for 100 h in the Al-0.22Zr alloy. Figure 6a is a frequency histogram showing the dispersion of the measurements, indicating a

Precipitation Evolution and Modeling of Growth Kinetics of L1$_2$-structured Al$_3$Zr Particles in Al-0.22Zr and
Al-0.32Zr (wt.%) Alloys Isothermally Aged

1605

(a)   **(b)**
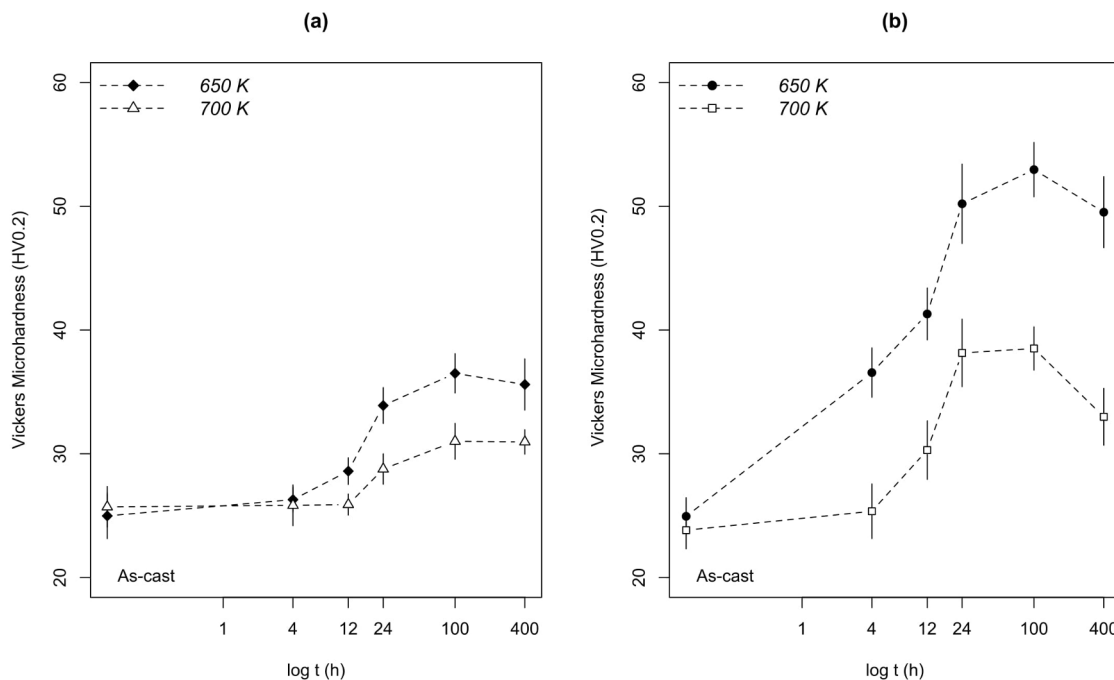
Figure 5. Variation of microhardness values as a function of aging time at the temperatures of 650 and 700K for the (a) Al-0.22Zr and (b) Al-0.32Zr alloys.

Table 2. Particle measurement results.

Alloy	Aging condition	Region of dendrite branch	< r > (nm)	Nº of images	Particles counted
Al-0.22Zr	650 K 100 h	Center	7 ± 1	10	239
	650 K 400 h	Center	7 ± 2	3	74
	650 K 400 h	Periphery	106 ± 21	10	183
	700 K 100 h	Center	12 ± 1	10	596
Al-0.32Zr	650 K 100 h	Center	3 ± 0.4	4	111
	650 K 400 h	Center	5 ± 1	5	62
	650 K 400 h	Periphery	19 ± 4	3	43

unimodal distribution of measurements. Figure 6b is a box-whisker diagram, which is useful in showing the dispersion of data and identification of outliers.

4.3.1 Al-0.22Zr Alloy

Figure 7 presents TEM images of the Al-0.22Zr alloy aged at distinct conditions. Figure 7a is a dark-field image of the center of a dendritic branch after aging at 650 K for 100 h, with particles presenting ⟨r⟩ = 7 ± 1 nm. Figure 7b is a dark-field image of a sample aged at 700 K for 100 h at the center of a dendritic branch, with larger particles: ⟨r⟩ = 12 ± 1 nm. Figure 7c is also a dark-field image of a sample aged at 650 K for 400 h. It is possible to observe that there are finer particles at the center of the dendrite branches, with ⟨r⟩ = 7 ± 2 nm and larger particles at the periphery of the

dendrite branches, exhibiting ⟨r⟩ = 107 ± 21nm. Figure 7d is the bright-field image of Figure 7c it is possible to observe the interactions of dislocations and precipitates. At the left corner of the image dislocations are bowing between particles, a process characteristic of the Orowan mechanism[41]. At the right corner of the image, precipitates present a straight line, which are possibly due to the interaction of dislocation gliding in different planes with Al$_3$Zr precipitates.

As particles in samples aged for 100 h are smaller at 650 K than at 700 K (Figures 7a and 7b, respectively), microhardness values are greater after aging at the former condition (Figure 5a). Although after 400 h of aging at 650 K there are large particles at the periphery of the dendrite branches, microhardness values presented a small decrease only. It is possible that the number density of larger precipitates is much lower than at the center of dendrite
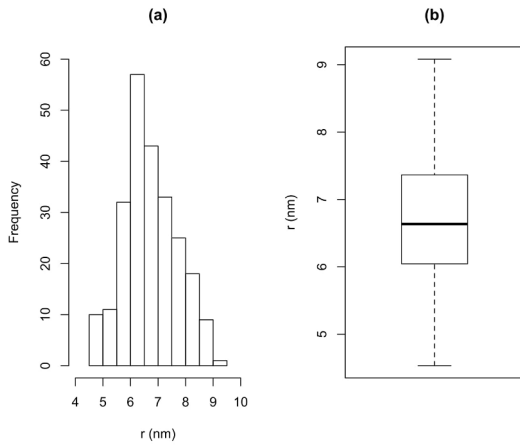
Figure 6. Dispersion of precipitate radii in a sample aged at 650 K for 100 h: (a) frequency histogram and (b) box-whisker plot.

branches, provided that the latter particles are capable of maintaining appreciable hardening. The work of Ness[8], in which an Al-0.18Zr alloy was aged at 733 K for 700 h, did not reported the presence of differences between particles at the center and periphery of dendrite branches even though aging temperatures and times were more elevated than in the

present study. The author reported the continuous growth of the particles following a diffusional growth law from Ham[8].

Aged samples presented fine $L1_2$-structured Al_3Zr precipitates in its microscructure. Figure 8a is a bright-field image of a sample aged at 700 K for 100 h. The diffraction conditions highlight mostly the Al matrix and dislocations, which are overlapping precipitates. At the top left of the micrograph, the blank area is the perforation caused by electropolishing.

Figure 8b is a dark-field image of Figure 8a. It shows nanometer-scale particles homogeneously distributed through the matrix. The dark-field image uses the (010) superlattice reflection, which is characteristic of $L1_2$-structured Al_3Zr precipitates. At the top left of Figure 8b the SADP of the image exhibits a [103] zone axis, where {020} reflections belong to the Al matrix. Manual indexing of the SADP and simulations using the WEB-E MAPS software[42], were realized to confirm the structure of the particles. In Figure 8b, arrows indicate precipitates which are also shown in Figure 8c, a complementary dark-field image using a ($0\bar{2}0$) reflection, highlighting matrix interactions, possibly due to dislocations. Precipitate particles in this aging condition present an average mean radius - $\langle r \rangle$ = 12 ± 1 nm. Figure 8d is a bright-field image of the same region in Figure 8a,
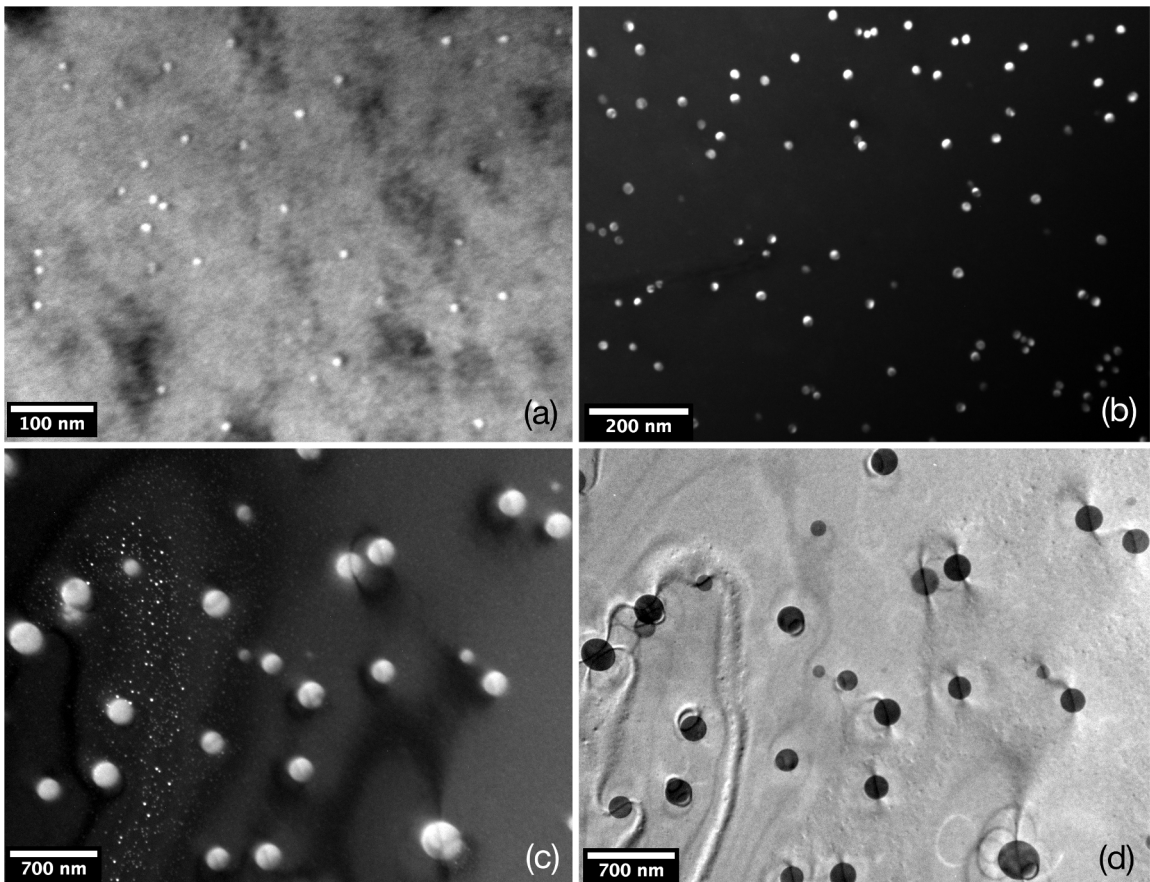
Figure 7. TEM images of an Al-0.22Zr alloy: (a) dark-field micrograph of sample aged at 650 K for 100h; (b) dark-field, aged at 700 K for 100 h; (c) dark-field, aged at 650 K for 400 h; (d) bright-field image of Fig.7c.
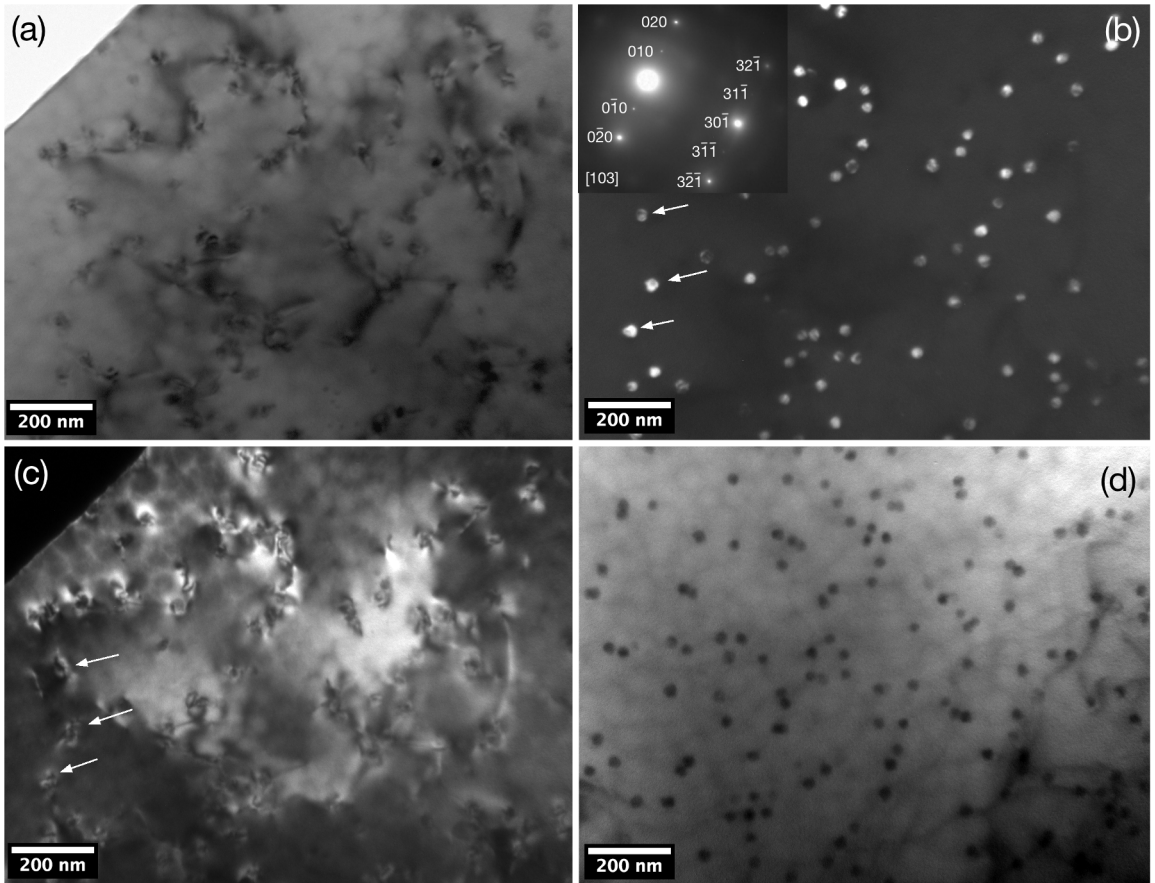
Figure 8. TEM micrographs of the Al-0.22Zr alloy aged at 700 K for 100 h. (a) bright-field image, (b) complementary dark-field image of Fig.8a, (c) complementary dark-field image of Fig.8a and (d) tilted bright-field image.

using tilting of the sample, thus highlighting precipitate particles only.

Figures 9 a and b are bright-field images in diffraction conditions showing the Ashby-Brown contrast, characteristic of coherent particles[43]. It is possible to qualitatively judge particle coherency by the loss of symmetry of the coherency strains between precipitate and matrix, i.e. the straight black lines along particles transform to a stripped pattern and the upper and lower lobes become asymmetrical[6,44], what was not observed in the present study.

Eq. 14[8] gives the absolute precipitate/matrix mismatch - δ, where a_0 = 4.0495 Å[45] and a_p=4.08 Å[8] are the lattice parameters of Al and Al$_3$Zr L1$_2$, respectively, resulting in δ =0.75%, a value that indicates elevated coherency[5]. During aging, as particles grow there is a threshold size over which, precipitates start to lose coherency. The number of atomic planes necessary for the loss of coherency - n, is in Eq.15[30]. Considering the spacing between {200} planes, the Al$_3$Zr precipitates should remain coherent to n = 130 planes, what corresponds to a radius of 26 nm[6], thus indicating that excluding the particles at the periphery of dendrite branches in samples aged at 650 K for 400 h, the other particles observed in this study remain coherent.

$$\delta = 2\left| a_0 - a_p / a_0 + a_p \right| \qquad (14)$$

$$n = 1/\delta \qquad (15)$$

Figure 10a is a bright-field image of precipitates along dislocations; Figure 10b presents its complementary superlattice dark-field micrograph, using {100} reflections. The sample was aged at 700 K for 100 h. It is possible to observe that precipitates present protuberances, possibly due to growth instabilities on solute depleted regions[6]. In the studies of Knipling et al.[6] and Ness[8], instabilities were observed in solute depleted regions after aging at 698 K and 733 K, respectively.

Growth instabilities do not appear at the center of dendrite branches. This is because this phenomenon occurs due to solute gradients at the precipitate/matrix interface, as a result of the difference in solid solubility due to the Gibbs-Thomson effect. This difference in solid solubility occurs when any oscillation (spherical harmonic) perturbs the spherical particle. As at the center of dendrite branches the number density of particles is greater, the overlapping of its diffusion field reduces solute gradients, thus stabilizing particle interface[30].
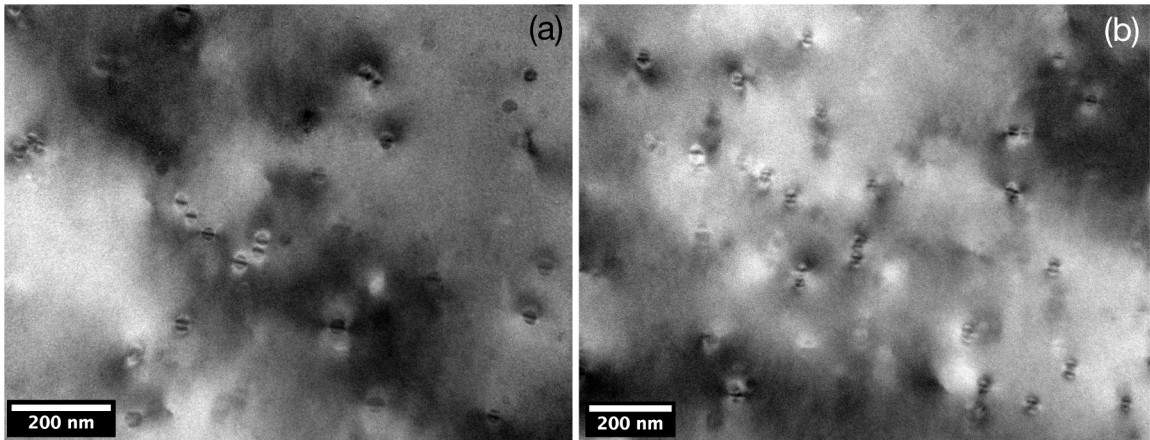
Figure 9. (a) and (b) Bright-field image of a sample aged at 700 K for 100 h, with Al$_3$Z precipitates, exhibiting the Ashby-Brown coherency strain contrast
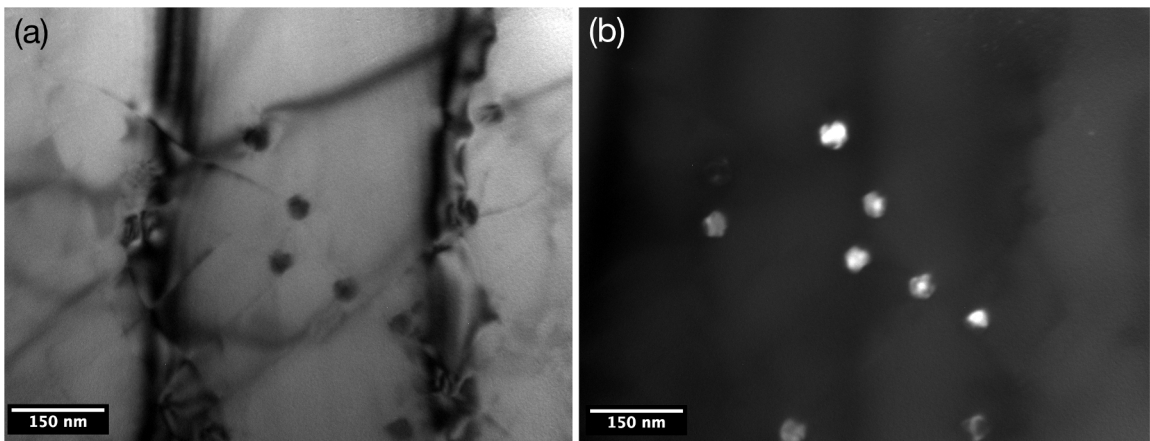
Figure 10. (a) Bright-field image of an interdendritic region in sample aged at 700 K for 100 h and (b) complementary dark-field image.

In the present study, no growth instabilities emerged in samples aged at 650 K on particles at the periphery of dendrite branches, as shown in Figure 7c. Aging at lower temperatures is usually associated with the formation of more interface instabilities, once diffusion is slower and the elimination of solute gradients is more difficult[30].

4.3.2 Al-0.32Zr Alloy

Figure 11a is a bright-field image of an Al-0.32Zr alloy aged at 650 K for 100 h. homogeneously distributed spherical Al$_3$Zr precipitates are present, exhibiting $\langle r \rangle$ = 3±0.4nm. The SADP of the image indicates the presence of L1$_2$-structured Al$_3$Zr particles due to the presence of {110} reflections and the orientation indicates a [1T0] zone axis. Figure 11b is a micrograph of the center of a dendrite branch of a sample aged at 650 K for 400 h. Its SADP image also indicates the presence of L1$_2$-structured Al$_3$Zr precipitates, which exhibit $\langle r \rangle$ = 5 ± 1 nm, Figure 11c is its complementary superlattice dark-field image, using {100} reflections and Figure 11d its axial superlattice dark-field image with the (100) reflection.

The nucleation of Al$_3$Zr particles in the hyperperitectic alloy provided a higher increase in hardening at peak strength condition (100 h at 650K) than in the more dilute alloy, due to the precipitation of finer particles.

Figure 12a shows the edge of a dendrite branch in sample aged at 650 K for 400 h. It is possible to observe that near the center of the dendrite branch (lower right corner), particles present smaller radius, while towards the edge of the dendrite branch (upper left corner), particles present an increase in radius. Figure 12b, shows the periphery of dendrite branches, where particles exhibit $\langle r \rangle$ = 19 ± 4 nm. In these regions, there are "rod-like" Al$_3$Zr particles, as indicated by arrows. These particles nucleate in solute depleted zones and present L1$_2$-structured Al$_3$Zr precipitates[6,8].

Figure 13a is a bright-field micrograph of a sample aged at 650 K for 400 h at the center of dendrite branches. It is possible to observe L1$_2$-structured Al$_3$Zr precipitates near a dislocation. The precipitates present antiphase boundaries - APBs, parallel to each other, as indicated by arrows. Figure 13b, a complementary dark-field image of Figure 13a,

Precipitation Evolution and Modeling of Growth Kinetics of L1$_2$-structured Al$_3$Zr Particles in Al-0.22Zr and Al-0.32Zr (wt.%) Alloys Isothermally Aged

1609
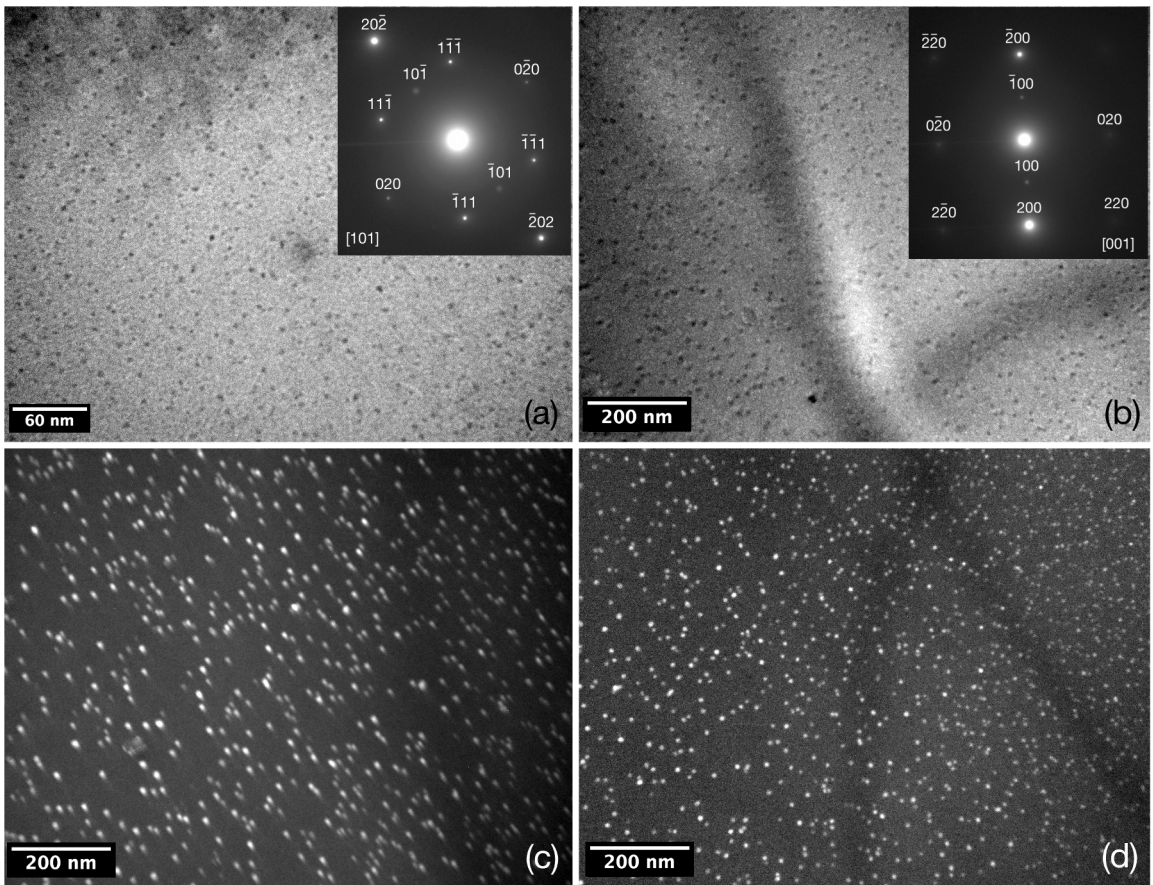
Figure 11. (a) Bright-field micrograph with SADP of a dendritic region in an Al-0.32Zr alloy aged at 650 K for 100 h and (b) for 400 h, both showing fine Al$_3$Zr L1$_2$ precipitates. (c) and (d) are superlattice dark-field and axial superlattice dark-field images.
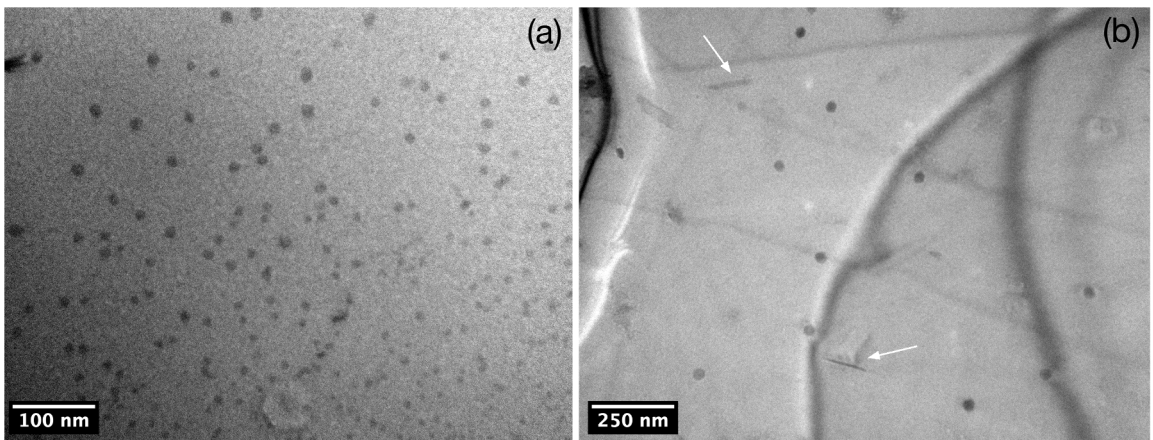
Figure 12. TEM bright-field micrograph of (a) edge of a dendrite and (b) an interdendritic region in an Al-0.32Zr alloy aged at 650 K for 400 h, exhibiting spherical and rod-like (arrows) Al$_3$Zr L1$_2$ precipitates.

also exhibits these structures. Their presence indicates the beginning of the L1$_2 \rightarrow$ D0$_{23}$ transition, in which an antiphase boundary is formed along {100} planes, with a $\vec{v}$=a/2$\langle$110$\rangle$ dislocation vector[14,29,46] and the Al$_3$Zr precipitate changes its structure from face centered cubic (metastable) to tetragonal (stable), although its stoichiometry remains unchanged[47].

In the present study, no characteristic D0$_{23}$-structured Al$_3$Zr reflections were observed in the SADP with APBs, as {004}, {103} or {105}[9]. In the work of Knipling et al.[6], the presence of antiphase boundaries was also observed in spherical particles of samples aged after 400 h, at the temperatures of 648 K, likewise in the present study, the
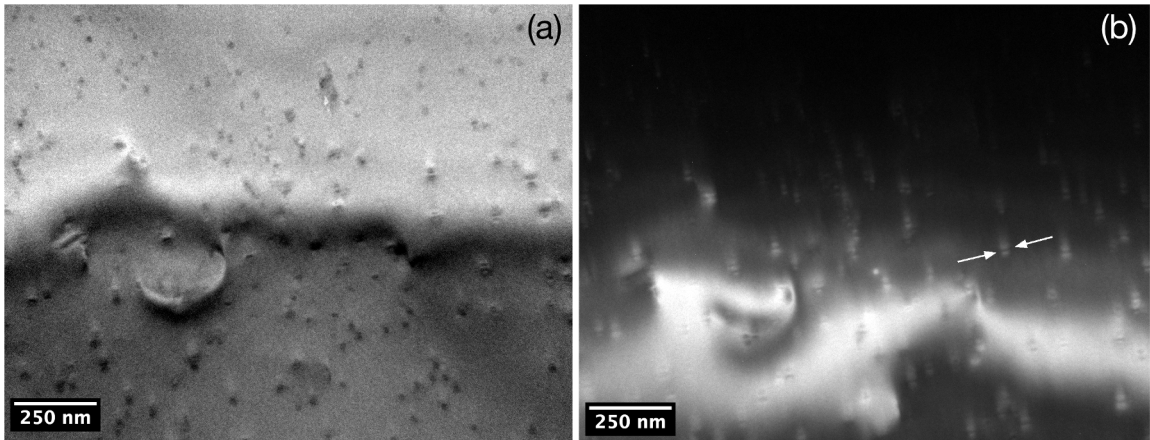
Figure 13. Micrographs of an Al-0.32Zr alloy aged at 650 K for 400 h showing precipitates with antiphase boundaries near a dislocation, (a) bright-field and (b) dark-field image (APBs indicated by arrows).

authors identified the particles as the L1$_2$ *strukturbericht* and the presence of D0$_{23}$ reflections is not observed.

4.3.3 Microstructural evolution

Figure 14 summarizes the main measurement results of ⟨r⟩ for the studied alloys after aging at 650 K. In Figure 14a, there are results for the center of the dendrite branches, while in Figure 14b, the results are from the periphery of the dendrite branches. It is possible to observe that in the later regions ⟨r⟩ values are bigger than in the former, what is predicted in Eq 4, using the concentration profiles from Eq.1, which are shown in Figure 15, using the fitted values of k_0 =1.48 and k_0= 1.76 for the Al-0.22Zr and Al-0.32Zr alloys, respectively. It is possible to observe that even in the more dilute alloy, at the center of dendrite branches the predicted composition is almost twice the nominal Zr composition.
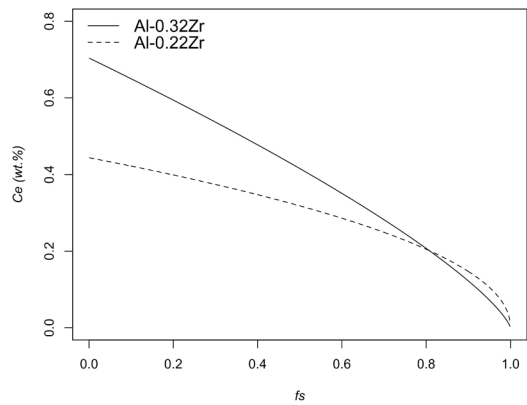
Figure 15. Solute segregation during solidification as a function of the solidified fraction $-f_s$ for the Al-0.22Zr and Al-0.32Zr alloys.
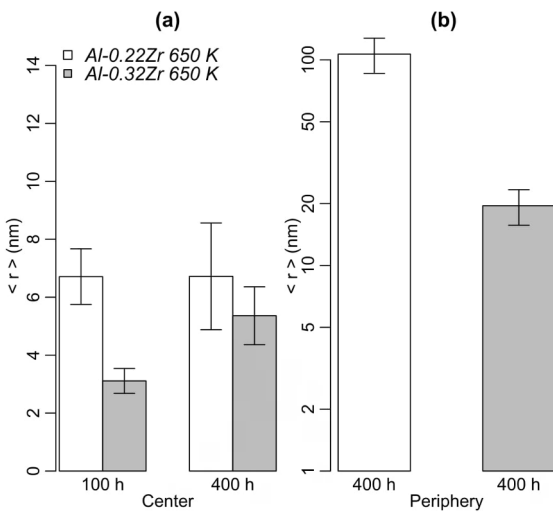
Figure 14. Variation of the precipitate mean radii in the studied alloys at different aging conditions in both (a) center and (b) periphery of dendrite branches.

The difference in solute content along the dendrite branches will promote particles with distinct r* (Eq.4). Results of r* for the Al-0.22Zr and Al-0.32Zr alloys at 650 K are presented in Figure 16. It is possible to observe that at the center of dendrite branches (lower f_s values) low r* occur for both alloys, with the Al-0.22Zr presenting slightly greater r*, resulting from its lower solute content. Towards the periphery of dendrite branches (higher f_s values), r* values increase progressively reaching values such as 28 nm for the Al-0.22Zr alloy. At a given f_s, Zr content is so low, provided no nucleation occurs.

The precipitates at the center of dendrite branches, Al-0.32Zr alloy in Figure 14a, presented an increase in ⟨r⟩ during aging between 100 and 400 h, although in the Al-0.22Zr alloy precipitate radii remained constant.

Eq.7 shows that the greater Ω, the greater r_d for a given temperature and time. As Ω must be greater in the Al-0.32Zr alloy, possibly this is the reason why the experimental increase

Precipitation Evolution and Modeling of Growth Kinetics of L1$_2$-structured Al$_3$Zr Particles in Al-0.22Zr and Al-0.32Zr (wt.%) Alloys Isothermally Aged

1611
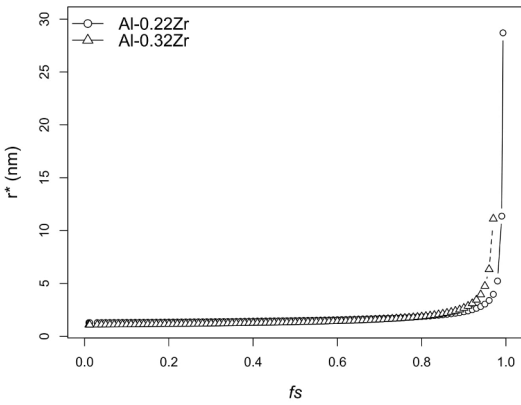
Figure 16. Critical radius for nucleation at 650 K for the Al-0.22Zr and Al-0.32Zr alloys.

in radius is greater than in the Al-0.22Zr alloy at the center of dendritic branches (Figure 14a). In the latter alloy, the difference in precipitate radii between the center and periphery of dendrite branches is greater than in the Al-0.32Zr alloy. Considering the Gibbs-Thomson effect, the solute content in the matrix near the smaller precipitates will be greater than near the biggest particles[30,35]. This will create concentration gradients that lead to solute diffusion in the direction of the largest particles[30,35], therefore reducing Ω at the center of dendrite branches. This difference in solute concentration as a function of particle radius is expressed in Eq. (12)[35]. This mechanism is characteristic of coarsening, where volume diffusion controls the process (Lifschitz-Sliozov-Wagner - LSW theory) (Eq.16), where r_0 is the precipitate radius at the onset of coarsening and k_r the coalescence rate[30,35]. In this mechanism, the larger particles drain solute from the smaller ones, provided the former increase in size[35].
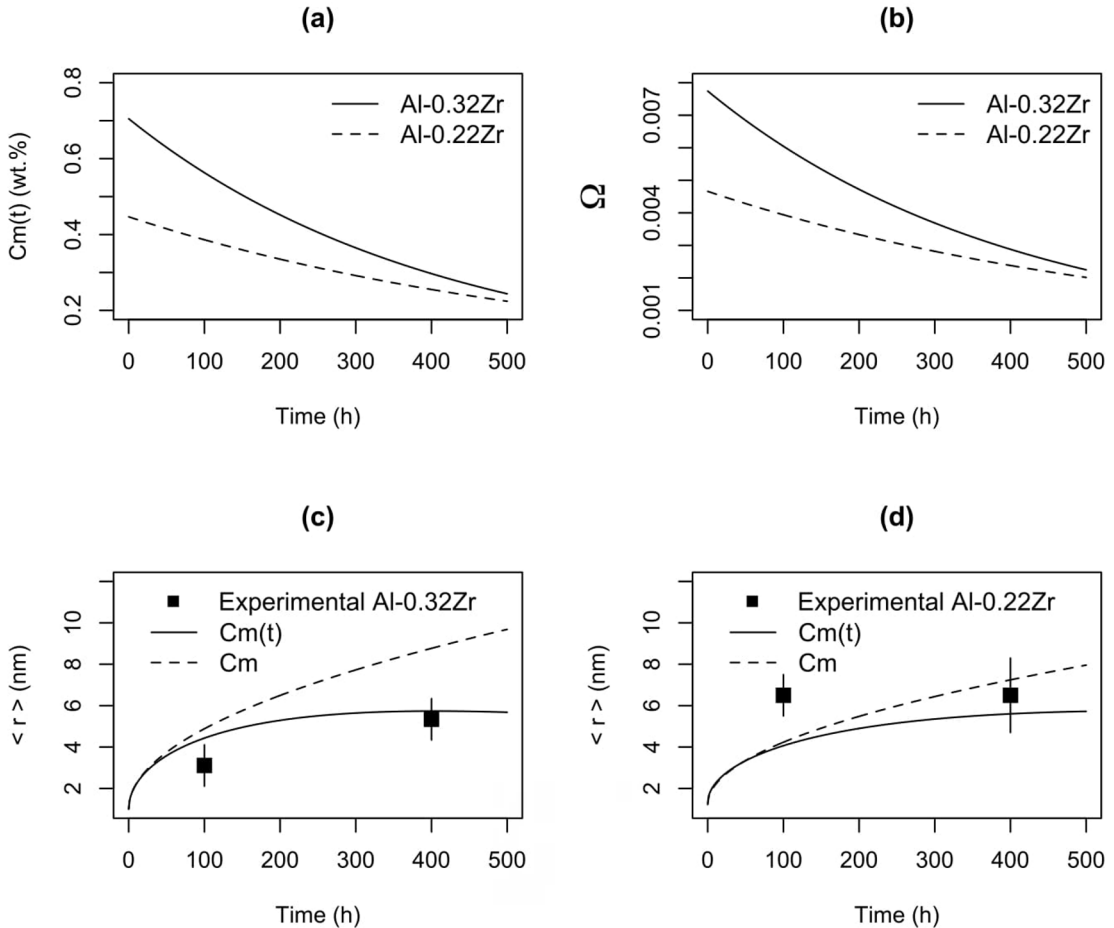
Figure 17. (a) Variation of solute at the center of the dendrite branches during aging at 650 K, (b) variation of Ω during aging, (c) evolution of precipitate radius in the Al-0.32Zr alloy during aging and (d) variation of precipitate radius with time in the Al-0.22Zr alloy.

$$r^3 - r_0^3 = k_r\left(t - t_0\right) \qquad (16)$$

Figure 17a presents the results for Eq. (10). It is possible to observe that during aging at 650K, the solute content in both the Al-0.32Zr and Al-0.22Zr alloys (full and dashed lines, respectively) decreases with aging time, due precipitation evolution. Besides having a greater Zr concentration, the Al-0.32Zr alloy present a lower interparticle spacing, thus increasing the Zr consumption during aging, for particle growth.

The reduction in Zr content in the matrix, therefore, reduces the supersaturation at the center of dendrite branches (Figure 17b), reducing the potential for particle growth of the Al-0.32Zr and Al-0.22Zr alloys (Figures 17c and d, respectively).

In Figure 17c, the model (full line, Eq.13) predicts an increase in radius (r_m) that is also observed experimentally, resulting in a low RSS for the Al-0.32Zr alloy (RSS = 1.79). The dashed line C_m is the prediction of particle growth without solute loss due to precipitation. In Figure 17d, the predicted increase in radius is lower than in Figure 17c, largely due to the lower Ω. The experimentally observed precipitate radii presented a negligible increase comparing with the Al-0.32Zr alloy. The goodness of fit reduced due to the greater residual at 100 h of aging. The RSS in this case is greater: RSS = 7.78. It is possible that in the Al-0.22Zr alloy, the nucleation of larger particles at the periphery of dendrite branches has caused an overall depletion of solute during aging, increasing r*, that, consequently presents a lower potential for growth.

5. Conclusions

- Microhardness presented greater values after heat-treatment at 650 K in both alloys, where peak microhardness occurred after 100 h and presented a slight decrease after 400 h. At 650 K finer L1$_2$-structured Al$_3$Zr particles were nucleated, in comparison with aging at 700K.
- The Al-0.32Zr alloy presented a finer precipitate distribution than the more dilute alloy after aging at 650 K at the center and periphery of dendrite branches;
- The difference between ⟨r⟩ of precipitates at the center and periphery of dendrite branches is greater in the Al-0.22Zr alloy, due to the lower solute content and greater r* at the periphery of dendrite branches, this disparity increases during aging possibly due to solute gradients and solute migration in the direction of the larger particles;
- During aging at 650 K of the Al-0.22Zr alloy, precipitates at the center of dendrite branches presented the same mean precipitate radius at 100 and 400 h, this is because of solute loss for the larger particles at the periphery of dendrite branches that are hindering growth and promoting competitive

growth. At the Al-0.32Zr alloy, both process are possibly occurring, although the supersaturation is greater, increasing the potential for diffusional growth;
- Due to its sizes, it is possible to infer that L1$_2$-structured Al$_3$Zr precipitates remained coherent until 400 h after aging at 650 or 700 K at the center of dendrite branches, although at the periphery of dendrite branches, after aging at 650 K for 400 h particles presented ⟨r⟩ = 107 nm, over the threshold value for the loss of coherency;
- The experimental results of the increase in precipitate radius presented overall goodness of fit with the theoretical values for diffusional particle growth.

7. References

1. Booth-Morrison C, Dunand DC, Seidman DN. Coarsening resistance at 400 ºC of precipitation-strengthened Al-Zr-Sc-Er alloys. *Acta Materialia*. 2011;59(18):7029-7042.

2. Kaufman JG, Rooy EL. Aluminum Casting Alloys. In: Kaufman JG, Rooy EL. *Aluminum Alloy Castings: Properties, Processes and Applications*. Materials Park: ASM International; 2004. p. 7-20.

3. Zhou WW, Cai B, Li WJ, Liu ZX, Yang S. Heat-resistant Al-0.2Sc-0.04Zr electrical conductor. *Materials Science and Engineering: A*. 2012;552:353-358.

4. Knipling KE, Dunand DC, Seidman DN. Nucleation and Precipitation Strengthening in Dilute Al-Ti and Al-Zr Alloys. *Metallurgical and Materials Transactions A*. 2007;38(10):2552-2563.

5. Knipling KE, Dunand DC, Seidman DN. Criteria for developing castable, creep-resistant aluminum-based alloys - A review. *Zeitschrift für Metallkunde*. 2006;97(3):246-265.

6. Knipling KE, Dunand DC, Seidman DN. Precipitation evolution in Al-Zr and Al-Zr-Ti alloys during isothermal aging at 375-425 ºC. *Acta Materialia*. 2007;56(1):114-127.

7. Du XD. Study on ageing and creep of Al-0.1Zr alloy. *Materials Science and Engineering: A*. 2006;432(1-2):84-89.

8. Ness E. Precipitation of the metastable cubic Al$_3$Zr-phase in subperitectic Al-Zr alloys. *Acta Metallurgica*. 1972;20(4):499-506.

9. Ohashi T, Ichikawa R. A new metastable phase in rapidly solidified Al-Zr alloys. *Metallurgical Transactions*. 1972;3(8):2300-2302.

10. Ness E, Billdal H. Non-equilibrium solidification of hyperperitectic Al-Zr alloys. *Acta Metallurgica*. 1977;25(9):1031-1037.

11. Ryum N. Precipitation and recrystallization in an Al-0.5wt.%Zr-Alloy. *Acta Metallurgica*. 1969;17(3):269-278.

12. Chaudhury ZA, Suryanarayana C. A TEM study of decomposition behavior of a melt-quenched Al-Zr alloy. *Metallography*. 1984;17(3):231-252.

13. Knipling KE, Dunand DC. Creep resistance of cast and aged Al-0.1Zr and Al-0.1Zr-0.1Ti (at.%) alloys at 300-400 ºC. *Scripta Materialia*. 2008;59(4):387-390.

14. Zedalis MS, Fine ME. Precipitation and ostwald rippening in dilute Al Base-Zr-V alloys. *Metallurgical Transactions A*. 1986;17(12):2187-2198.

15. Hatch JE. Constitution of Alloys. In: Hatch JE, ed. *Aluminum: Properties and Physical Metallurgy*. Metals Park: American Society for Metals; 1984. p. 25-57.

16. Knipling KE, Dunand DC, Seidman DN. Precipitation evolution in Al-Zr and Al-Zr-Ti alloys during aging at 450-600 ºC. *Acta Materialia*. 2008;56(6):1182-1195.

17. Zhang Y, Zhou W, Gao H, Han Y, Wang K, Wang J, et al. Precipitation evolution of Al-Zr-Yb alloys during isochronal aging. *Scripta Materialia*. 2013;69(6):477-480.

18. Zhang Y, Gao H, Kuai Y, Han Y, Wang J, Sun B, et al. Effects of Y additions on the precipitation and recrystallization of Al-Zr alloys. *Materials Characterization*. 2013;86:1-8.

19. Booth-Morrison C, Seidman DN, Dunand DC. Effect of Er additions on ambient and high-temperature strength of precipitation-strengthened Al-Zr-Sc-Si alloys. *Acta Materialia*. 2012;60(8):3643-3654.

20. Vlach M, Cizek J, Melikhova O, Stulikova I, Smola B, Kekule T, et al. Early Stages of Precipitation Process in Al-(Mn-)Sc-Zr Alloy Characterized by Positron Annihilation. *Metallurgical and Materials Transactions A*. 2015;46(4):1556-1564.

21. Lefebvre W, Masquelier N, Houard J, Patte R, Zapolsky H. Tracking the path of dislocations across ordered Al$_3$Zr nano-precipitates in three dimensions. *Scripta Materialia*. 2014;70:43-46.

22. ASTM International. *ASTM E348 - Standard Test Method for Knoop and Vickers Hardness of Materials*. West Conshohocken: ASTM International; 2011.

23. Ünlü N. Preparation of high quality Al TEM specimens via a double-jet electropolishing technique. *Materials Characterization*. 2008;59(5):547-553.

24. Garcia A. Redistribuição de Soluto. In: Garcia A. *Solidificação: Fundamentos e Aplicações*. 2ª ed. Campinas: Unicamp; 2007. p. 57-80.

25. Barbetta PA, Reis MM, Bornia AC. Correlação e Regressão. In: Barbetta PA, Reis MM, Bornia AC. *Estatística para Cursos de Engenharia e Informática*. Florianópolis: Editora UFSC; 2010. p. 308-346.

26. Robson JD, Prangnell PB. Dispersoid precipitation and process modelling in zirconium containing commercial aluminium alloys. *Acta Materialia*. 2001;49(4):599-613.

27. Clouet E, Nastar M, Sigli C. Nucleation of Al$_3$Zr and Al$_3$Sc in aluminum alloys: from kinetic Monte Carlo simulation to classical theory. *Physical Review B*. 2004;69(6):064109.

28. Abbaschian R, Abbaschian L, Reed-Hill RE. Appendices. In: Abbaschian R, Abbaschian L, Reed-Hill RE. *Physical Metallurgy Principles*. 2nd ed. Stamford: Cengage Learning; 2009. p. 731.

29. Chen YC, Fine ME, Weertman JR. Microstructural evolution and mechanical properties of rapidly solidified Al-Zr-V alloys at high temperatures. *Acta Metallurgica et Materialia*. 1990;38(5):771-780.

30. Doherty RD. Diffusive transformations in the solid state. In: Cahn RW, Haasen P, eds. *Physical Metallurgy*. 4th ed. Amsterdam: Elsevier Science; 1996. p. 1363-1505.

31. Porter DA, Easterling KE. Diffusion. In: Porter DA, Easterling KE. *Phase Transformations in Metals and Alloys*. 2nd ed. London: Chapman & Hall; 1992. p. 60-109.

32. Hirano K, Fujikawa S. Impurity diffusion in aluminum. *Journal of Nuclear Materials*. 1978;69-70:564-566.

33. Shewmon PG. Diffusion Equation. In: Shewmon PG. *Diffusion in Solids*. London: McGraw-Hill; 1963. p. 1-39.

34. Guo Z, Sha W. Quantification of Precipitation Hardening and Evolution of Precipitates. *Materials Transactions*. 2002;43(6):1273-1282.

35. Porter DA, Easterling KE. Diffusional Transformations in Solids. In: Porter DA, Easterling KE. *Phase Transformations in Metals and Alloys*. 2nd ed. London: Chapman & Hall; 1992. p. 263-313.

36. Medina SF, Ruiz-Bustinza I, Robla J, Calvo J. Theoretical and Experimental Nucleation and Growth of Precipitates in a Medium Carbon-Vanadium Steel. *Metals*. 2017;7(2):45.

37. Allen CM, O'Reilly KAQ, Cantor B, Evans PV. Intermetallic phase selection in 1XXX Al alloys. *Progress in Materials Science*. 1998;43(2):89-170.

38. Desch PB, Schwarz RB, Nash P. Formation of metastable L1$_2$ phases in Al$_3$Zr and Al-12.5%X-25%Zr (X = Li, Cr, Fe, Ni, Cu). *Journal of the Less Commom Metals*. 1991;168(1):69-80.

39. Hori S, Saji S, Takehara A. Metastable phase and grain refinement in rapidly solidified Al-Zr alloys. *Journal of Japan Institute of Light Metals*. 1981;31(12):793-797.

40. Knipling KE, Seidman DN, Dunand DC. Ambient- and high-temperature mechanical properties os isochronally aged Al-0.06Sc, Al-0.06Zr and Al-0.06Sc-0.06Zr (at.%) alloys. *Acta Materialia*. 2011;59(3):943-954.

41. Russel AM, Lee KL. Strengthening Mechanisms. In: Russel AM, Lee KL. *Structure-Property Relations in Nonferrous Materials*. Hoboken: John Wiley & Sons; 2005. p. 28-37.

42. Zuo JM, Mabon JC. Web e-MAPS, On-line Software for Electron Diffraction Analysis. Available from: <http://emaps.mrl.uiuc.edu>. Access in: 8/8/2017.

43. Fultz B, Howe JM. Diffraction Contrast in TEM Images. In: Fultz B, Howe JM. *Transmission Electron Microscopy and Diffractometry of Materials*. 3rd ed. New York: Springer; 2008. p. 377-422.

44. Iwamura S, Miura Y. Loss in coherency and coarsening behavior of Al$_3$Sc precipitates. *Acta Materialia*. 2004;52(3):591-600.

45. Zedalis M, Fine ME. Lattice parameter variation of Al$_3$ (Ti, V, Zr, Hf) in Al-2AT.% (Ti, V, Zr, Hf) alloys. *Scripta Metallurgica*. 1983;17(10):1247-1251.

46. Ryum N. Precipitation in an Al-1.78 wt % Hf alloy after rapid solidification. *Journal of Materials Science*. 1975;10(12):2075-2081.

47. Knipling KE. *Development of a Nanoscale Precipitation-Strengthened Creep-Resistant Aluminum Alloy Containing Trialuminide Precipitates*. [PhD thesis]. Evanston: Northwestern University; 2006. 241 p.